

1 Implications of differences between recent anthropogenic aerosol emission inventories 2 on diagnosed AOD and radiative forcing from 1990 to 2019

3 Marianne T. Lund^{1,*}, Gunnar Myhre¹, Ragnhild B. Skeie¹, Bjørn H. Samset¹, Zbigniew Klimont²

4

5 1 CICERO Center for International Climate Research, Oslo, Norway

6 2 International Institute for Applied Systems Analysis (IIASA), Laxenburg, Austria

7 *Corresponding author: m.t.lund@cicero.oslo.no

8

9 **Abstract**

10 *This study focuses on implications of differences between recent global emissions inventories for*
11 *simulated trends in anthropogenic aerosol abundances and radiative forcing (RF) over the 1990-2019*
12 *period. We use the ECLIPSE version 6 (ECLv6) and Community Emission Data System year 2021*
13 *release (CEDs21) as input to the chemical transport model OsloCTM3 and compare the resulting*
14 *aerosol evolution to corresponding results derived with the first CEDs release, as well as to observed*
15 *trends in regional and global aerosol optical depth (AOD). Using CEDs21 and ECLv6 results in 3%*
16 *and 6% lower global mean AOD compared to CEDs in 2014, primarily driven by differences over China*
17 *and India, where the area average AOD is up to 30% lower. These differences are considerably larger*
18 *than the satellite-derived interannual variability in AOD. A negative linear trend over 2005-2017 in*
19 *global AOD following changes in anthropogenic emissions is found with all three inventories but is*
20 *markedly stronger with CEDs21 and ECLv6. Furthermore, we confirm that the model better captures*
21 *the sign and strength of the observed AOD trend over China with CEDs21 and ECLv6 compared to*
22 *using CEDs, while the opposite is the case for South Asia. We estimate a net, global mean aerosol-*
23 *induced RF in 2014 relative to 1990 of 0.08 W m⁻² for CEDs21, and 0.12 W m⁻² for ECLv6, compared*
24 *to 0.03 W m⁻² with CEDs. Using CEDs21, we also estimate the RF in 2019 relative to 1990 to be 0.10*
25 *W m⁻², reflecting the continuing decreasing trend in aerosol loads post 2014. Our results facilitate more*
26 *rigorous comparison between existing and upcoming studies of climate and health effects of aerosols*
27 *using different emission inventories.*

28

29 **1 Introduction**

30 Human activities have led to a substantial increase in atmospheric abundances of aerosols relative to
31 pre-industrial conditions. While increasing emissions of greenhouse gases is the dominant driver of
32 recent global warming, aerosols play a key role in shaping regional and global climate, and for
33 anthropogenic climate change, through their interactions with radiation and clouds. The sixth assessment
34 report (AR6) of the Intergovernmental Panel on Climate Change (IPCC) estimates that changes in
35 atmospheric aerosols have contributed an effective radiative forcing (ERF) of -1.3 W m^{-2} over the
36 industrial era (1750–2014), albeit with a wide uncertainty range of -2.0 to -0.6 W m^{-2} (Forster et al.,
37 2021).

38 Over recent decades, anthropogenic emissions of aerosols and their precursor gases have changed
39 rapidly, with substantial spatiotemporal heterogeneity, particularly in Asia. Following decades of rapid
40 economic growth in China, the combustion of coal, other fossil fuels, and biofuels increased
41 considerably, resulting in the region becoming the dominant source of air pollution emissions. However,
42 since the adoption of the national action plans targeting particulate matter levels (i.e. Air Pollution

43 Prevention and Control in 2013 (SCPRC, 2013) and Winning the Blue Sky Defense Battle in 2018
44 (SCPRC, 2018)), emissions of sulfur dioxide (SO₂) and then nitrogen oxide (NO_x) in China have
45 declined rapidly (Klimont et al., 2017; Klimont et al., 2013; Tong et al., 2020; Zheng et al., 2018).
46 Recent studies suggest that also black carbon (BC) emissions are declining (Kanaya et al., 2020; Zheng
47 et al., 2018). A strong growth in emissions of SO₂ and other pollutants has been seen in South Asia
48 (Kurokawa & Ohara, 2020), resulting, according to studies, in India overtaking China as the dominant
49 emitter of SO₂ (Li et al., 2017). These contrasting trends have given rise to a distinct dipole pattern of
50 increasing and declining aerosol optical depth over South and East Asia, respectively, visible in satellite
51 data (Samset et al., 2019). Such rapid changes are likely to affect the climate of the regions, as aerosols
52 have been shown to have a notable influence on regional temperature and precipitation, including
53 extremes (e.g. Bollasina et al., 2011; Hegerl et al., 2019; Marvel et al., 2020; Samset et al., 2018;
54 Sillmann et al., 2013), with different responses to scattering and absorbing aerosols. However, the exact
55 nature and magnitude of such climate implications need to be better quantified (Persad et al., 2022).

56 Robust quantification of the impacts of aerosols requires reliable and consistent estimates of
57 anthropogenic emissions. However, currently there exist substantial differences, in both magnitudes and
58 trends, between available emission inventories (e.g. Crippa et al., 2018; Elguindi et al., 2020; Smith et
59 al., 2022). Emission inventories are quantifications of contributions from various industrial processes or
60 other anthropogenic activities to the rate of emissions of various compounds to the atmosphere. They
61 generally combine bottom-up information such as reported economic activities with direct observations
62 and process modelling and are used extensively in essentially all efforts to quantify climate and air
63 quality implications of human activities. While the overall scientific uncertainty on aerosol-induced
64 global mean radiative forcing (RF) is larger than the estimated regional changes, the uncertainty also
65 varies over the recent decades depending on the overall level of emissions and their location relative to
66 cloud decks and other climate features (Bellouin et al., 2020; Regayre et al., 2014; Samset et al., 2019;
67 Szopa et al., 2021). Hence, understanding both the inherent inventory differences and the implications
68 of these on downstream calculations and modelled quantities such as aerosol optical depths and radiative
69 forcing is crucial.

70 As an example, a critical issue that has recently been highlighted is a notable underestimation of the
71 decline in Chinese emissions of SO₂ and NO_x, and overestimation of carbonaceous aerosol emissions
72 in Asia and Africa, in the Community Emission Data System (CEDS) developed for the sixth cycle of
73 the Coupled Model Intercomparison Project (CMIP6) (Szopa et al., 2021). Recent work has shown that
74 results from the CMIP6 experiments fail to fully capture the observed recent trends in aerosol optical
75 depth (AOD) in Asia (Cherian & Quaas, 2020; Ramachandran et al., 2022; Su et al., 2021; Wang et al.,
76 2021), with the discrepancy largely attributed to the misrepresentation of emissions in the region in last
77 decade of the historical CMIP6 period. Other studies demonstrate that the poor representation of
78 observed aerosol trends can propagate to further uncertainties in attribution of aerosol-induced impacts,
79 such as the East Asian monsoon (Wang et al., 2022) and health impacts (Cheng et al., 2021). In addition
80 to CMIP6, the CEDS emissions have also been used in individual model studies of historical aerosol
81 evolution, radiative forcing, sector attribution, and air quality assessments (e.g. Bauer et al., 2020;
82 Chowdhury et al., 2022; Lund et al., 2018; Lund et al., 2020; Paulot et al., 2018). Moreover, uncertainties
83 and biases in the baseline historical inventory may influence scenario-based assessments of near-term
84 future regional climate risk.

85 Since the initial parts of the CMIP6 exercise, the CEDS inventory has undergone several revisions. The
86 most recent version from 2021, covering the period up to 2019, exhibit several key differences compared
87 to the initial release – for some species all the way back to the early 2000s. More specifically, emissions
88 of BC, OC and NO_x are all substantially lower in the update, in global totals and, particularly, in Asia,
89 and the decreasing trend in Chinese SO₂ is more pronounced. However, the implications of these
90 differences in input data on simulated anthropogenic aerosol distributions, globally and regionally, and
91 the resulting radiative forcing, have not been fully quantified and cannot be directly extrapolated.

92 Furthermore, as the update to CEDS came too late for uptake in IPCC AR6, it is pertinent to ask if the
93 influence of these emission inventory differences affected the assessed evolution of atmospheric aerosol
94 trends and subsequent climate implications.

95 Here, we present an investigation of the implications of known differences in recent emission inventories
96 on quantified aerosol burdens, optical depth, and radiative forcing, over the period 1990-2019. Using
97 the chemical transport model OsloCTM3, we perform simulations with the CEDS21 emission inventory
98 and compare to previously published results derived with the original CEDS release (Lund et al., 2018;
99 Lund et al., 2019). We also perform simulations with a third recent global inventory, the ECLIPSE
100 version 6b, where emissions are similar in evolution but generally even lower than in CEDS21,
101 especially in the most recent period. We explore the differences in simulated evolution of global and
102 regional anthropogenic aerosol loads between experiments using the different inventories, comparing
103 optical depth to remote sensing observations, and quantify the resulting radiative forcing. Our aims are
104 to document the model ability to represent recent observed aerosol trends and to quantify the
105 implications of differences in inventories available for the community on downstream diagnosed
106 quantities critical for assessing the air quality and climate implications of anthropogenic aerosol.

107

108 **2 Methods**

109 Atmospheric concentrations of aerosols are simulated with the global chemical transport model
110 OsloCTM3 (Lund et al., 2018; Søvde et al., 2012). The model is driven by meteorological data from the
111 European Center for Medium Range Weather Forecast (ECMWF) OpenIFS model updated every 3
112 hours and is run in a $2.25^\circ \times 2.25^\circ$ horizontal resolution, with 60 vertical levels (the uppermost centered
113 at 0.1 hPa). OsloCTM3 treats tropospheric and stratospheric chemistry, as well as modules for
114 carbonaceous, secondary organic, sulfate, ammonium-nitrate, sea salt and dust aerosols. Aerosols are
115 scavenged by convective and large-scale rain (ice and liquid phase), with rainfall calculated from
116 ECMWF data for convective activity, cloud fraction, and rainfall. Dry deposition applies prescribed
117 deposition velocities for different land cover types. For further details we refer to Lund et al. (2018) and
118 Søvde et al. (2012).

119 The aerosol optical depth (AOD) and instantaneous top-of-atmosphere radiative forcing due to aerosol-
120 radiation interactions (RF_{ari}) is calculated offline using a multi-stream model with the discrete ordinate
121 method DISORT (Myhre et al., 2013; Stamnes et al., 1988). The same radiative transfer model is also
122 used to estimate the radiative forcing of aerosol-cloud interactions (RF_{aci}) (earlier denoted the cloud
123 albedo effect or Twomey effect). To account for the change in cloud droplet concentration resulting
124 from anthropogenic aerosols, which alter the cloud effective radius and thus the optical properties of the
125 clouds, the approach from Quaas et al. (2006), is used. Briefly, this approach is based on a statistical
126 relationship between cloud droplet number concentrations and fine-mode AOD derived from satellite
127 data from the MODerate Resolution Imaging Spectroradiometer (MODIS).

128 Modeled AOD is compared with retrievals from the MODIS instrument on the Aqua satellite, which is
129 available for the period 2003-2020 (MOD08, 2018). We use the combined Dark Target and Deep Blue
130 AOD at 550nm, release MOD08_M3_V6.1, downloaded from the NASA Giovanni interface. MODIS-
131 Terra AOD is also available for the same period and is, for most years, around 10% lower than MODIS-
132 Aqua on global average. However, based on previous evaluation of the MODIS AOD and a reported
133 drift in the Terra data (Levy et al., 2010; Sherman et al., 2017), we choose to use MODIS-Aqua for the
134 model comparison in the current study. Temporal trends in simulated and observed AOD are estimated
135 on global-mean and grid point basis by linear least square fitting and defined as statistically significant
136 (from no trend) when the linear Pearson's correlation coefficient is significant at the 0.05 level. To

137 minimize the influence of individual years, e.g. with higher biomass burning influence, we calculate a
138 set of trends with one and one year removed from the sample and then take the average of this set of
139 coefficients. Interannual variability is estimated on a grid point basis as the standard deviation of the
140 residual when subtracting a 10-year boxcar average (with mirrored data around the end points). We also
141 compare modeled AOD with ground-based measurements from the AERONET (AErosol RObotic
142 NETwork) (Holben et al., 1998) Version 3 Level 2.0 retrievals at 500 nm. The comparison uses all
143 available data from all months and stations for a given year, with modeled AOD linearly interpolated to
144 the latitude and longitude of each station.

145
146 Five different time series of simulated aerosol distributions covering the 1990-2019 period are included
147 in this analysis, using three different emission inventories and either fixed or actual (i.e. corresponding
148 to the emission year) meteorology. The fixed meteorology runs forms the basis for investigating
149 differences in simulated anthropogenic aerosol and corresponding RF, while the latter is used in the
150 comparison with observed AOD. Table 1 provides a summary of the experiments.

151
152 Two sets of fixed meteorology simulations are performed using anthropogenic emissions from CEDS
153 version 2021 (O'Rourke et al., 2021) (hereafter "*CEDS21*") and ECLIPSEv6b baseline (hereafter
154 "*ECLv6*") inventories. The ECLv6 emissions are developed with the Greenhouse Gas - Air Pollution
155 Interactions and Synergies (GAINS) model (Amann et al., 2011). Version 6b (IIASA, 2022) consists of
156 gridded aerosol and reactive gas emissions in 5-year intervals over the period 1990-2015, as well as
157 emissions for 2008, 2009, 2014 and 2016. The Community Emission Data System (CEDS) inventory
158 provides a gridded inventory of anthropogenic greenhouse gas, reactive gases and aerosols since 1750
159 (Hoesly et al., 2018). In the first release, the most recent year was 2014, while the 2021 release covers
160 the period until 2019. Simulations are performed for 1990, 1995, 2000, 2005, 2010, 2014 and 2016
161 emissions, as well as years 2018 and 2019 for CEDS21. Results from the current study are compared
162 with previously published results from simulations over 1990 to 2014 performed with the first release
163 of the CEDS emissions (hereafter "*CEDS*") (Lund et al., 2018) and three of the SSP scenarios (SSP1-
164 1.9, SSP2-4.5, and SSP3-7.0) from 2015 to 2100 (here we use data for 2020 and 2030) (Lund et al.,
165 2019). These three scenarios broadly span the range of aerosol and precursor emissions projected in the
166 SSPs. Keeping in line with the experimental design in Lund et al. (2018), we use year 2010
167 meteorological data and each simulation is run for one year, with 6 months spin-up. All three time series
168 uses biomass burning emissions from van Marle et al. (2017) from 1990 to 2014 and Global Fire
169 Emissions Database version 4 (GFED4, Randerson et al. (2017)) thereafter. We note that van Marle et
170 al. (2017) emissions are also based on GFED. Other natural emissions (dust and sea salt aerosols,
171 precursor gases from the ocean, soil, and vegetation) are fixed at the year 2010 levels.

172
173 For the comparison with MODIS data, we use a timeseries of OsloCTM3 simulations with CEDS
174 emissions and actual meteorology covering the period 1990-2017 (the last three years uses Shared
175 Socioeconomic Pathways (SSP) 2-4.5 emissions (Fricko et al., 2017) linearly interpolated between 2015
176 and 2020) (hereafter "*CEDSmet*"). These simulations were originally performed for the phase III of the
177 AeroCom project (e.g. Glib et al., 2021). For the present study, we also produce an updated version
178 covering the 2001-2017 period using CEDS version 2021 emissions (hereafter "*CEDS21met*"). While
179 differences in emissions exist also in the years prior, we restrict the use of resources by only going back
180 to the start of the MODIS record, covering the period when the differences are most pronounced. In
181 these simulations, the other natural aerosol emissions also vary following the meteorological year.

182
183
184 **3 Results and discussion**

185 Here we first document the differences in simulated global and regional aerosol abundances and trends
186 arising from the spread between emission inventories. We then investigate how AOD diagnosed from
187 experiments using old and new emission estimates compare with observed AOD. Finally, we present
188 updated estimates of radiative forcing relative to 1990.

189

190 **3.1 Influence of emission inventory differences on simulated aerosol distributions**

191 Figure 1 shows global, total emissions of SO₂, BC, OC, NO_x, ammonium (NH₃) and non-methane
192 volatile organic compound (NMVOC) over the 1990-2019 period in the inventories used here. The
193 differences are particularly pronounced after 2005. Both ECLv6 and CEDS21 show substantially lower
194 emissions of most species during this period, relative to CEDS. In 2014, the largest relative differences
195 between CEDS21 and CEDS are in BC and OC emissions, where CEDS21 is 20-30% lower. For SO₂,
196 NO_x, and NMVOC, the corresponding number is approximately 10%. ECLv6 is generally lower than
197 both CEDS inventories, particularly for SO₂ and NMVOC, by about 30%. While not used in this study,
198 we also note that similar differences have also been found between CEDS and two other recent global
199 inventories, the Emissions Database for Global Atmospheric Research (EDGAR) version 5 (Crippa et
200 al., 2020) and Hemispheric Transport of Air Pollution (HTAP) version 3 (Crippa et al., 2022).

201

202 Important geographical distinctions underlie these global differences, as demonstrated in Fig. S1 for
203 selected main source regions. While a comprehensive investigation of causes for the inventory
204 differences is beyond the scope of the present study, and can be difficult due to the number of underlying
205 assumptions, input data, and revisions, we discuss some key features here. All three inventories rely on
206 the energy statistical data from International Energy Agency (IEA), however, there are differences in
207 assumptions about emission rates, implementation of policies, and data on non-energy sources. The
208 ECLv6 estimates include explicit representation of air quality policies, and their implementation
209 efficiency, drawing on national information and, if not available, extrapolation of trends considering
210 capacity replacement (e.g., new vehicles, newly build power plant capacity) and emission performance
211 of these new technologies. The result is, among other things, estimated faster decline of SO₂ and NO_x
212 emissions from power and industry (in turn in total emissions) in China over recent years than in CEDS
213 (Fig. S1a,d). This decline has been also confirmed in Zheng et al. (2018). CEDS21 made a correction to
214 CEDS, mirroring the estimates in the GAINS model for ECLv6. In South Asia, dominated by India,
215 ECLv6 and CEDS21 show a similar difference to CEDS emissions of SO₂ and NO_x, representing use
216 of updated emission characteristics for coal power plants. India has had a slower economic growth and
217 less heavy industry than China. While some policies aimed at controlling NO_x from transport has been
218 introduced, the limited polices in the power and industry sector have resulted in increasing Indian SO₂
219 and NO_x emissions, but the growth has been slower than that in China in the 2000's. For BC and OC
220 (Fig. S1b,c), the largest inventory differences are found in East Asia, mainly China, owing to differences
221 in estimates of emissions from coal use in industry, with ECLv6 applying the lowest emission factors,
222 and from open burning of municipal waste. For the latter category, CEDS has originally relied on the
223 rather high estimates of waste generation and share burned (using Wiedinmyer et al. (2014)), while
224 ECLv6 used independently estimated generation rates (Gómez-Sanabria et al., 2022). The declining BC
225 trends in East Asia, as shown in ECLv6 and CEDS21, have been supported by measurements (e.g.
226 Kanaya et al., 2020). Estimates for some species, e.g., NH₃, are often based on very similar sources of
227 information as, apart from in Europe and North America, these have received less attention from policy
228 making and measurement (emissions) community. Consequently, estimates are similar across all
229 inventories at the aggregated regional level (Fig. S1e). Aside from East and South Asia, the overall

230 temporal evolution is generally similar in the main source regions across inventories, although
231 magnitudes can differ.

232

233 3.1.1 Global and regional aerosol burdens in 2014

234 The differences between inventories are substantial enough to influence simulated aerosol burdens (i.e.
235 column integrated aerosol mass, in mg m^{-2}) at the global mean level. For 2014, i.e. the most recent
236 common year for all three emission inventories, we estimate 4% and 8% lower global mean burdens of
237 total BC when using CEDS21 and ECLv6 (6% and 11% if considering only aerosols only from fossil
238 fuel and biofuel combustion), respectively, compared to CEDS (Table S1). For primary organic aerosol
239 (POA), the corresponding numbers are 11% and 13% (30% and 40%), while global mean total sulfate
240 burden is 8% and 15% lower with CEDS21 and ECLv6. Smaller reductions in the order of 3-4% are
241 also seen in the global mean SOA burden. Biogenic VOC emissions, the main source of SOA, are the
242 same in all simulations. However, the SOA abundance is affected by the lower emissions of
243 anthropogenic VOCs in both CEDS21 and ECLv6 than in CEDS (Fig.1), as well as by lower amount of
244 POA, which serve as substrates for SOA formation.

245 For all these aerosol species, the burden differences are consistently largest over East Asia, followed by
246 South Asia, and larger for ECLv6 than for CEDS21. Figure 2 shows absolute regional mean burden
247 (with corresponding relative changes given in Fig.S3). Regions considered are East Asia (EAS), South
248 Asia (SAS), Sub-Saharan Africa (SAF), North America (NAM), South America (SAM), North Africa
249 and the Middle East (NAF), Europe (EUR), Southeast Asia (SEA), and Russia (RBU) (see also Fig. S2).
250 For EAS, the new simulated burden of BC and POA is 30-40% lower, depending on inventory,
251 compared to simulations using CEDS, following 50-60% lower BC and OC emissions. The 40-50%
252 lower SO_2 emissions translate to 20-30% lower regional sulfate burden in our simulations. A similar
253 relationship between emission and burden differences are simulated for SAS, where the burdens of BC,
254 POA, and sulfate are 6%, 27%, and 30% lower, respectively, in experiments with ECLv6 than with
255 CEDS. Lower burdens of sulfate and POA are simulated for all other regions as well, and in particular
256 over NAF with ECLv6. In some regions, like SAM, NAF, and SAF, the new inventories estimate 20-
257 30% lower BC emissions than CEDS, however, due to the lower absolute magnitudes, the simulated
258 burden differences are small compared to other aerosols. We note that regional burdens can be
259 influenced by long-range transport and thus affected by inventory differences outside the main source
260 region. We also note that we find differences in surface concentrations between simulations that are
261 broadly similar to the burden changes. While beyond the scope of the present study, this may have
262 implications for assessments of air pollution related health impacts.

263 The only species that is globally more abundant in simulations with the two new inventories is nitrate.
264 There is considerable regional heterogeneity, where the burden is lower compared to the CEDS
265 experiments in South Asia and on the US east coast but higher in the US Midwest, parts of Africa and
266 South America, and, especially, over East Asia (Fig.2, Fig.S3). While absolute differences are small in
267 many regions compared to other species, the net effect is nevertheless a 15 and 24% higher global mean
268 nitrate burden with CEDS21 and ECLv6, respectively, compared to using CEDS emissions. Changes in
269 the atmospheric nitrate distribution result from a complex interplay between differences in emissions of
270 NO_x , NH_3 , and SO_2 . Studies have also shown that nitrate formation can be influenced by background
271 concentrations of VOCs (e.g. Womack et al., 2019) We find the largest absolute difference in nitrate in
272 EAS and SAS, however, of opposite sign. In EAS, emissions of SO_2 and NO_x are both lower in ECLv6
273 and CEDS21 than in CEDS, whereas NH_3 emissions are higher (Fig.1, Fig.S1). This results in lower
274 chemical competition for available sulfate and, in turn, enhanced formation of nitrate aerosol. In SAS,
275 SO_2 , NO_x , and NH_3 are all lower in the two new inventories than in CEDS, as is the nitrate burden.
276 Differences in concentrations of VOCs in the simulations with different inventories is a further
277 complicating factor. Studies have suggested that nitrate formation can be more sensitive to changes in

278 VOCs than NO_x, however, this is highly site specific (Yang et al., 2022). Further delineating the role of
279 individual factors on nitrate differences would require simulations beyond what is available for the
280 current study. The potential for an increasing relative role of nitrate for air pollution and climate in a
281 world with concurrent declines in SO₂ and NO_x emissions but little in NH₃ has also been discussed in
282 previous studies (e.g. Bauer et al., 2007; Bellouin et al., 2011; Zhai et al., 2021). However, while more
283 studies have focused on local air pollution impacts of nitrate, and associated mitigation strategies, nitrate
284 is still missing from many global climate models. Moreover, when included, the model diversity in
285 simulated distributions is large (Bian et al., 2017). Our results suggest that uncertainties in emissions
286 and choice of inventory can contribute to spread in simulated nitrate aerosols and confound the
287 comparison of conclusions across modeling studies. Moreover, the complexity of the nitrate response
288 demonstrates that the impact of inventory differences on simulated aerosols cannot be understood from
289 scaling with the changes in individual emissions but requires explicit modeling.

290 To place the range in estimates between simulations with different inventories into more context, we
291 compare the differences in simulated aerosol burdens in 2014 to the difference in burdens over the 5-
292 year period from 2014 to 2019 using CEDS21. Both globally and regionally, the spread in burdens
293 between simulations with different inventories and the 2014-2019 burden changes are of the same order
294 of magnitude. In other words, at least in this case, the changes resulting from inventory differences are
295 as large as those due to the recent overall change in anthropogenic emissions.

296 Combined, these burden differences translate to a 3% and 6% lower global, annual mean AOD with
297 CEDS21 and ECLv6, respectively, compared to CEDS in 2014 in our simulations. As expected, the
298 differences are most pronounced over China and India (Fig. S4), where we estimate 20% and 30% lower
299 regional mean AOD in 2014 using the two new emission inventories, respectively, compared to using
300 CEDS. For context, Fig. S4 also shows the interannual variability in AOD from MODIS-Aqua (see Sect.
301 2): In these regions the differences between inventories are markedly larger than what can be expected
302 from natural year-to-year variations.

303

304 3.1.2 Global and regional AOD 1990-2019

305 Next, we take a closer look at differences in the simulated temporal trend, focusing on total AOD. Figure
306 3 shows the global and regional mean AOD from 1990 to 2019. Also shown is the linear trend from
307 2005 to 2017 for each of the timeseries. This period overlaps with the availability of remotely sensed
308 AOD discussed in Sect. 3.1.3, as well as the period with the most pronounced inventory differences.
309 However, as there is a certain extent of inventory differences prior to 2005, we also provide
310 corresponding linear trends over the full 1990-2017 period in Table S2.

311 The simulated AOD is consistently lower when using CEDS21 and ECLv6 emissions compared to
312 CEDS over the full period studied, with increasing divergence over time, especially after 2005. We
313 estimate a significant (at the 0.05 level - see Sect. 2) negative linear trend in global mean AOD of -0.005
314 and -0.006 per decade in simulations with CEDS21 and ECLv6, respectively. This trend strengthens
315 when extended to 2019 based on simulations with CEDS21. A negative global trend is also found when
316 using the first CEDS release, however, it is smaller and not significant over the period 2005-2014.
317 Extending the timeseries to 2017 by assuming that emissions follow SSP2-4.5 after 2014 (see Sect. 2),
318 as in Fig. 3, the negative trends strengthens and switches to significant as per our definition, but it
319 remains weaker than for the other two inventories. Considering the full period, we estimate a significant
320 negative trend in simulations with CEDS21 and ECLv6, but no trend when using CEDS (Table S2).
321 This long-term decline in total AOD is primarily driven by the decline in sulfate AOD, following the
322 emission decline after introduction of air quality policies, first in the US and Europe, then in China, and
323 the collapse of the Soviet Union (e.g. Aas et al., 2019). Over the full period, we simulate increasing
324 trends in BC and nitrate AOD, significant at the 0.05 level, with all three inventories (not shown),

325 however, their contributions to total AOD are much smaller than that of sulfate. Robust evidence of a
326 declining influence by aerosols on climate since 1990 was recently found from observables (Quaas et
327 al., 2022). Our model simulations capture this overall trend, and the findings reinforce the role of
328 changes in anthropogenic emission, particularly since 2005. Furthermore, we suggest that if using the
329 original CEDS emissions, models may have failed to capture this trend. We note that biomass burning
330 emissions also change over time in our simulations, but we do not find any significant trend in biomass
331 aerosols (BC and POA) AOD on the global mean scale over this period. We do note that years of high
332 biomass burning activity, such as 2019 where GFED4 emissions are 25% higher than in 2018, can lead
333 to marked jumps in simulated AOD. We have limited possible influence of such years on the linear trend
334 calculated (see Sect. 2).

335 Regionally, we simulate significant declining trends in AOD over 2005-2017 for EUR and NAM, with
336 this trend extending back to 1990 (Table S2), as expected. This is also consistent with surface
337 observations both AOD and atmospheric sulfur and in agreement with other models (Mortier et al.,
338 2020; Aas et al., 2019), and we capture the decline regardless of which emission inventory is used. In
339 both regions, and across simulations with all three scenarios, we find a decline in the AOD of BC, OA,
340 and sulfate, but an increasing trend in nitrate AOD. Over RBU, we also simulate a decline a significant
341 decline in area average AOD over the full 1990-2017 period, but a flatter evolution when considering
342 only 2005-2017. However, the results are similar with all three scenarios also here. In parts of the RBU
343 region, GFED4 shows an increase in emissions over the latter period, resulting in a positive trend in the
344 AOD of biomass aerosols from 2005. On the African continent, we simulate negative, albeit weak, trend
345 in AOD over the 2005-2017 period for SAF. In contrast, the trend over the full period is positive.
346 Anthropogenic emissions in SAF have increased (Fig. S1), although less steeply than in Asia, and we
347 find significant increases in the AOD of all the anthropogenic species with all inventories from 1990 to
348 2017. However, from 2005 onwards, there has been a decreasing trend in GFED4 emissions, following
349 a reduction in the burnt area of savannas (Wu et al., 2021). Biomass burning aerosols contribute
350 relatively more to total AOD here than in the northern hemisphere regions and hence impose a stronger
351 effect on the area average trend. A similar pattern is seen for SAM, while for SEA, another biomass
352 burning influenced region, we find less clear trends. While diagnosed trends in total AOD in these
353 regions are mostly of similar sign across simulations with the three inventories, we find that the trend in
354 sulfate AOD diverges between model runs using CEDS or CEDS21 (positive trend) and ECLv6
355 (negative trend) in SAF and NAF, pointing to a need to better understand the drivers of emission changes
356 in these regions and homogenize between inventories. As expected, the key differences between
357 simulations with different inventories arise over Asia. Simulations with both CEDS21 and ECLv6 show
358 a significant decreasing trend in total AOD over EAS between 2005 and 2017. While a decline is found
359 using CEDS, it is much weaker and not significant. Moreover, differences between inventories affect
360 the sign of the simulated trend when considering the full period, owing primarily to the spread in
361 estimated sulfate AOD. For SAS, we simulate a consistent positive trend, but ranging from 0.01 per
362 decade with ECLv6 to 0.03 per decade with CEDS, with increasing divergence in AOD over time.
363 Similar magnitude differences between the sets of experiments exist for the AOD of all anthropogenic
364 aerosol in this region.

365

366 3.1.3 Comparison with observed AOD

367 To explore whether the model captures observed global and regional trends better with the CEDS21
368 emissions than with CEDS, we compare simulated AOD to MODIS-Aqua retrievals and ground-based
369 AERONET measurement. For this evaluation, we also use simulations where the model is driven by
370 meteorology for the respective years, referred to as CEDSmet and CEDS21met (see Sect. 2), for more
371 realistic comparison with the observations. Using both these, we also estimate negative linear trends in
372 simulated global mean AOD from 2005 to 2017, strengthening from -0.001 per decade in CEDSmet to
373 -0.003 per decade in CEDS21met. These are, however, weaker than the trends derived from the fixed

374 meteorology simulations in Sect. 3.1.2 (Fig. 3) and not significant at the 0.05 level, demonstrating the
375 notable influence of variability in meteorology and natural aerosols, masking trends due to changes in
376 anthropogenic emissions. This influence is particularly visible for the area averaged AOD for SAF and
377 NAF, where the diagnosed trend is positive but non-significant in these simulations, in contrast to the
378 negative trend found in simulations with fixed meteorology above. The negative trend over SAM is also
379 not significant at the at the 0.05 level in these runs. For other focus regions, results are similar between
380 fixed and actual meteorology runs and significant trends arise over the natural variability.

381 Figure 4a shows the annual, global mean simulated AOD from 1990 to 2017 and the MODIS-Aqua
382 AOD from 2003 to 2019. Dashed lines show the linear 2005-2017 trends. Figures 4b-d show the spatially
383 explicit trends. We first note that the magnitude of simulated global mean AOD is lower than that
384 derived from MODIS-Aqua, by around 20%. However, the overall geographical pattern of the observed
385 AOD is captured by the model (Fig. S5). Furthermore, the AOD simulated by the OsloCTM3 is within,
386 although in the lower range, of the spread in AOD between the CMIP and AeroCom models (Vogel et
387 al., 2022). As also shown by Vogel et al. (2022), there can be a notable spread in AOD derived from
388 different satellite products. They found a 13% standard deviation range in global mean AOD between
389 eight satellite products, with MODIS retrievals in the upper end. Although again the lower range, the
390 OsloCTM3 AOD falls within the full range of the satellite-derived annual mean AOD. Overall, this
391 suggests a reasonable OsloCTM3 performance in terms of magnitude and distribution.

392 In terms of temporal evolution, MODIS-Aqua data indicates a very weak positive linear trend of 0.001
393 per decade in global mean AOD over the 2005-2017 period (0.004 per decade when extending the data
394 to 2019). We do not, however, find this trend to be significant. MODIS data is influenced by substantial
395 year-to-year variability, in particular after 2010, which was also pointed out by Vogel et al. (2022).
396 Regions of significant positive observed AOD trend include parts of the ocean in the southern
397 hemisphere (Fig. 4b). Here, sea salt aerosols could be causing the increase. However, Quaas et al. (2022)
398 recently showed that this positive trend is not clear in Multi-angle Imaging SpectroRadiometer (MISR)
399 data. While we are focused on the anthropogenically-influenced regions in the present analysis, we
400 briefly note that the magnitude of the trends over the southern hemisphere oceanic regions is also not
401 captured by the model (Fig. 4c-d). We also simulate weaker trends in the boreal regions of North
402 America and Russia, contributing to the model-observation difference.

403 Over the main anthropogenic emission sources regions, there are significant observed declines in AOD
404 over East Asia, US, and Europe (Fig. 4b). These trends have been confirmed by both ground based and
405 remote sensing observations of AOD and other variables (Gui et al., 2021; Moseid et al., 2020; Paulot
406 et al., 2018; Quaas et al., 2022). For NAM and EUR, we calculate an area average negative observed
407 trend of -0.006 and -0.009, respectively, from MODIS-Aqua. This is of the same sign but weaker than
408 the trend simulated with both emission inventories. For the latter, this contrast findings by Mortier et al.
409 (2020), where models in general were found to underestimate the observed decrease in AOD seen in
410 surface observations. Over EAS, where the influence of inventory differences is most pronounced, a
411 significant negative observed trend of -0.044 per decade is calculated. This is in very close agreement
412 with the -0.40 per decade AOD trend simulated with the CEDS21, while simulations with CEDS do not
413 show a significant trend. Hence, the model is clearly able to better represent observed trends with the
414 updated inventory. This is further confirmed in Fig. 5, where we show five-year average deviations from
415 the period 2003-2017 in both MODIS-Aqua and simulated AOD. Using CEDS21 results in marked
416 improvements compared to observed AOD trends over China, both for the first and most recent full 5-
417 year periods. However, the opposite tendency is found for AOD over SAS. Here observations suggest a
418 significant positive trend of 0.04 per decade. The diagnosed trends are also positive in simulations using
419 both inventories, but somewhat weaker, especially when switching from CEDS to CEDS21 (and even
420 more so when using EClv6 emissions - Fig.3). Figure 5 suggests that this discrepancy arises in the more
421 recent decade. Furthermore, simulated AOD, and underlying emissions, suggest a leveling off in recent
422 years, which is not seen from MODIS-Aqua. Whether this is due to inaccurate representation of the

423 evolution of anthropogenic emissions in the inventories or could be influenced by poor model
424 representation of other aerosols such as dust from agricultural soils and urban areas (e.g. construction,
425 non-exhaust transport emissions), is however not clear from this analysis. We note that the model
426 underestimates the magnitude of AOD observed by MODIS-Aqua in both EAS and SAS. To the extent
427 that the MODIS is accurate, this could support the latter. This type of dust is suggested to give an
428 important contribution to the particulate matter load (e.g. Chen et al., 2019; Xia et al., 2022), but are
429 still missing from many global models. Other contributing factors include the representation of
430 processes related to aerosol transport and scavenging. Finally, we also note that the 5-year deviations in
431 Fig. 5 show quite some variability over the Middle East, with both positive and negative deviations from
432 the baseline period. While anthropogenic emissions in this region increase steadily over the period (by
433 13-40% depending on species) in the inventories used in the present study, the strong influence from
434 dust emissions in this region likely dominates the temporal variability.

435 A previous OsloCTM3 study by Lund et al. (2018) found an improved agreement between year 2010
436 ground-based AERONET observations and model output, including over Asia, when switching from
437 CMIP5 and ECLIPSEv5 emissions to CEDS, the latter having higher emissions. This seemingly
438 contradicts expectations following the now-known biases in this first release of CEDS. Here we repeat
439 the comparison with AERONET, but for the year 2014. Resulting scatter density plots are given in Fig.
440 S6. The normalized mean bias (NMB) compared to AERONET ranges from -21 to -29% in the
441 simulations with fixed and actual meteorology. We find higher bias and lower correlation when
442 switching from the original CEDS release to CEDS21 and ECLv6. Hence, while the model is better able
443 to represent observed recent aerosol trends over East Asia with newer emission inventories, these results
444 point to other issues that may have been concealed by too high anthropogenic emissions. Dust and
445 atmospheric processing, as discussed above, are again possible contributing factors.

446

447 **3.2 Impact of inventory differences on estimated anthropogenic aerosol RF**

448 Finally, we quantify the aerosol-induced RF from the three sets of experiments. Figure 6a shows the
449 RFari, RFaci, and net aerosol radiative forcing (RFnet, RFari plus RFaci) relative to 1990 for the three
450 sets of experiments. The net RF of changes in anthropogenic (and biomass burning) aerosol is positive
451 since 1990, except for 1995 and 2005, where a small negative forcing is estimated. As shown in Fig. 1,
452 global anthropogenic SO₂ emissions show a peak in 2005 and the biomass burning emissions are
453 relatively high. This positive global mean net RF is determined mainly by the balance between a positive
454 forcing over the northern extratropics, dominated by aerosol-radiation interactions, and a negative
455 forcing over Asia and parts of South America and Africa with stronger contributions from aerosol-cloud
456 interactions (Fig. S7).

457 In 2014, we estimate a global mean RFnet of 0.03 W m⁻² for CEDS, 0.08 W m⁻² for CEDS21, and 0.12
458 W m⁻² for ECLv6 relative to 1990, of which the RFari constitutes 0.07 W m⁻², 0.09 W m⁻² and 0.10 W
459 m⁻², respectively. We note that our framework only captures the cloud albedo effect and not radiative
460 effects of any changes in cloud lifetime that may arise through the influence of aerosols (i.e. we calculate
461 RF, not ERF). Our RFari estimate using CEDS emissions is similar to the multi-model mean RFari of
462 0.05 W m⁻² derived for the 1990-2015 period using ECLIPSE version 5 emissions by Myhre et al.
463 (2017). The same study estimated a model mean RFnet of 0.1 W m⁻², but with a significant intermodel
464 spread, from close to zero to more than 0.2 W m⁻². This spread is larger than the difference between
465 estimates with different inventories in the present analysis. Nevertheless, the differences in emissions
466 between CEDS and CEDS21 (ECLv6) translates to a factor 3 (5) stronger RFnet in our calculations.

467 Figure 6b shows regional mean RF, including the balance between RFari and RFaci. Following the
468 significant decline in AOD over EUR and NAM, the dominant contributions to positive RF are found
469 here, followed by Russia. There is however little difference between simulations with three inventories.

470 In contrast, the net RF over EAS switches sign from negative in simulations with CEDS to positive
471 when using CEDS21 or ECLv6 due to observed decline in emissions now captured. While negative in
472 all three sets of experiments, the net RF over SAS is 40% (20%) weaker when ECLv6 (CEDS21)
473 emissions are used compared to CEDS. This results from a 50% (20%) lower net area averaged AOD
474 change between 1990 and 2014, compared to simulations with CEDS.

475 The CEDS21 inventory extends to 2019, compared to 2014 in CEDS. The global mean net RF over this
476 five-year period is estimated to be 0.10 W m^{-2} , driven primarily by a further positive forcing over China
477 in line with the continued decline in SO_2 emissions following implementation of measures targeting
478 improved air quality. Over India, the forcing in 2019 relative to 2014 remains negative, but weaker than
479 during the preceding period, while over Europe and western Russia, the RF is low suggesting little
480 further recent emission changes. We note however that this is a short period and results should be
481 interpreted with that in mind. Using a selection of the SSP scenarios, Lund et al. (2019) extended
482 simulations from 2014 CEDS emissions and quantified the projected aerosol-induced RF. The orange
483 hatched bars in Fig. 6 show the range in RFnet in 2020 and 2030 (relative to 1990) estimated with SSP1-
484 1.9, SSP2-4.5 and SSP3-7.0 in that study. The RFnet in 2019 estimated with CEDS21 here is close to
485 the lower end of the bar, i.e. the RFnet projected under SSP3-7.0. However, prior to this higher biomass
486 burning year, there are indications that the RFnet from simulations with CEDS21 tracked closer to SSP2-
487 4.5 or an even lower emission pathway.

488 The dipole pattern of aerosol changes, and resulting RF, over India versus China that can be seen in
489 observations and is expected to impose regional climate impacts, was first highlighted by Samset et al.
490 (2019). Using emissions from CEDS and SSP1-1.9, SSP2-4.5 and SSP3-7.0, combined with a radiative
491 kernel approach, that study estimated a range of 2014-2030 aerosol (SO_2 and BC) net RF of -1.0 W m^{-2}
492 (SSP1-1.9) to 0.82 W m^{-2} (SSP2-4.5) over India, and 0.06 W m^{-2} (SSP2-4.5) to 1.10 W m^{-2} (SSP3-7.0)
493 over China. Part of this range can be attributed to poor knowledge of current, and hence also future,
494 regional emissions (Samset et al. 2019). In the present study, we estimate regionally averaged RFnet in
495 2019 relative to 2014 of -0.09 W m^{-2} and 0.22 W m^{-2} over India and China, respectively. For China, this
496 recent RFnet is about 20% of the previously estimated difference between high and low future aerosol
497 emission scenarios in 2030 (SSP2-4.5 and SSP3-7.0). Missing or incorrectly captured past emission
498 trends can therefore markedly affect assessments of projected near-term aerosol-induced climate
499 impacts, as they depend on a well constrained starting point.

500

501 **4 Conclusions**

502 We have investigated the impact of differences between recent global emission inventories available for
503 the aerosol and climate modeling community on simulated anthropogenic aerosol abundances, and
504 associated radiative forcing, from 1990 to 2019. Simulations with the chemical transport model
505 OsloCTM3 and the CEDS emission inventory, developed for the sixth cycle of the IPCC, has been
506 compared with corresponding results using two newer inventories: The CEDS 2021 update (CEDS21)
507 and the ECLIPSE version 6b (ECLv6). Our objective was to evaluate the model performance
508 considering revisions to the emissions input data, partly done to correct known regional biases, and to
509 investigate the implications of inventory differences on downstream diagnosed quantities critical for
510 assessing the air quality and climate effects of anthropogenic aerosol.

511 We have found that, apart for nitrate, simulations with the CEDS21 (ECLv6) inventory give lower global
512 mean aerosol burdens than corresponding runs with CEDS, ranging from 4% (6%) for BC to approx.
513 10% (15%) for sulfate and POA in 2014 (the most recent historical year common for all scenarios).
514 Differences are consistently most pronounced over East Asia, followed by South Asia, where they are
515 on the order of 30–60% depending on species and scenario. Differences in the underlying anthropogenic
516 emissions arise from different assumptions about emission rates, data on non-energy sources, and,

517 importantly, representation of air quality policies and their implementation efficiency. In our model, the
518 global mean fine mode nitrate burden is 15% (24%) higher with CEDS21 (ECLv6) relative to CEDS,
519 but with regional heterogeneity in sign of the difference. Overall, we estimate 3% (6%) lower total AOD
520 with CEDS21 (ECLv6), respectively, compared to CEDS in 2014. The difference reaches approx. 20%
521 and 30% over East and South Asia.

522 Over East Asia, we diagnose a significant negative linear trend in total area averaged AOD from 2005
523 to 2017 of -0.03 per decade in simulations using the ECLv6 emissions. In contrast, we find no significant
524 trend in corresponding experiments with CEDS. Importantly, we find that the model is better able to
525 capture the trend observed by MODIS-Aqua with both new inventories. In all three sets of simulations,
526 we estimate a significant positive linear AOD trend over South Asia. The simulated trend is, however,
527 weaker than that derived from MODIS-Aqua and this gap increases when switching from CEDS to the
528 CEDS21 and ECLv6 inventories. We also underestimate the magnitude of observed AOD in the region,
529 at least compared to this specific satellite product. Recent emission trends are less well constrained by
530 observations in India than e.g. in China. The extent to which the model-observation difference arises
531 from the input of anthropogenic emissions or could be influenced by poor model representation of other
532 aerosols sources or atmospheric processes, is not clear from the present analysis. For other regions
533 considered, there is generally agreement in the sign of the simulated area averaged AOD trend between
534 the three sets of simulations, although the magnitude can differ, in particular for the AOD of individual
535 species. For instance, there is an increasing (over time) divergence in the sulfate AOD over Africa
536 between simulations using CEDS and ECLv6. Over most regions, nitrate AOD increases, however,
537 nitrate contributes relatively less to total AOD than sulfate and OA.

538 Using offline radiative transfer calculations, we estimate a global mean net aerosol RF in 2014 relative
539 to 1990 of 0.03 W m^{-2} for CEDS, 0.08 W m^{-2} for CEDS21, and 0.12 W m^{-2} for ECLv6. Regionally, the
540 sign of the net aerosol-induced RF switched from negative to positive when replacing CEDS emissions
541 with CEDS21 or ECLv6 in our study. Hence, the failure to capture recent observed emission trends in
542 China may have resulted in the wrong sign in estimates of the regional effect on the energy balance over
543 recent decades. Over South Asia, the area average net RF is up to 40% lower in simulations with the
544 updated inventories compared to CEDS.

545 While the focus of the present study is on anthropogenic aerosols, our comparison with observed AOD
546 reveals potential issues related to the representation of natural aerosols or other processes in the
547 OsloCTM3. In particular, the model does not capture the strength of the positive AOD trend observed
548 over high latitude North America and Russia, likely due to an increase in biomass burning aerosols. For
549 individual years, we also find a larger underestimation in AOD compared to AERONET measurements
550 when switching from CEDS to the lower CEDS21 and ECLv6 emissions, despite better representation
551 of some key regional observed trends. Further studies are required to investigate this in more detail.

552 Anthropogenic aerosols are changing rapidly, particularly in Asia, with potentially large but
553 insufficiently quantified implications for regional climate. We have demonstrated that differences
554 between recent emission inventories translate to notable differences in global and regional trends in
555 anthropogenic aerosol distributions, and in turn in estimates of radiative forcing. Although additional
556 studies are required to fully quantify the broader implications for aerosol-induced climate and health
557 impacts, our results facilitate comparisons between existing and upcoming studies, using different
558 emission inventories, of anthropogenic aerosols and their effects.

559

560 **Code availability**

561 The OsloCTM3 is available on from <https://github.com/NordicESMhub/OsloCTM3>.

562

563 **Data availability**

564 Model data underlying the manuscript figures are available from 10.6084/m9.figshare.20254764.
565 AERONET data is downloaded from <https://aeronet.gsfc.nasa.gov/>, MODIS data from
566 <https://giovanni.gsfc.nasa.gov/giovanni/>, and CEDS21 emissions from the PNNL DataHub
567 <https://doi.org/10.25584/PNNLDataHub/1779095>.

568

569 **Acknowledgements**

570 This work has been conducted with support from the Research Council of Norway (grants 248834,
571 314997 and 324182). The authors acknowledge the UNINETT Sigma2 – the National Infrastructure
572 for High Performance Computing and Data Storage in Norway – resources (grant NN9188K).

573

574 **Author contributions**

575 MTL led the study design and analysis and the writing. The OsloCTM3 model experiments were
576 performed by MTL and RBS. GM performed the radiative transfer modeling and BHS contributed
577 graphics, silly jokes, and MODIS analysis. All authors contributed to the discussions and writing.

578

579 **Competing interests**

580 The authors declare that they have no conflict of interest.

581

582

583

584 **References**

585

586 Bauer S. E., Koch D., Unger N., Metzger S. M., Shindell D. T. & Streets D. G. Nitrate
587 aerosols today and in 2030: a global simulation including aerosols and tropospheric ozone,
588 *Atmospheric Chemistry and Physics*. 7(19), 5043-5059, 2007.

589 Bauer S. E., Tsigaridis K., Faluvegi G., Kelley M., Lo K. K., Miller R. L., Nazarenko L.,
590 Schmidt G. A. & Wu J. Historical (1850–2014) Aerosol Evolution and Role on Climate Forcing Using
591 the GISS ModelE2.1 Contribution to CMIP6, *Journal of Advances in Modeling Earth Systems*. 12(8),
592 e2019MS001978, <https://doi.org/10.1029/2019MS001978>, 2020.

593 Bellouin N., Rae J., Jones A., Johnson C., Haywood J. & Boucher O. Aerosol forcing in the
594 Climate Model Intercomparison Project (CMIP5) simulations by HadGEM2-ES and the role of
595 ammonium nitrate, *Journal of Geophysical Research-Atmospheres*. 116, D20206,
596 10.1029/2011jd016074, 2011.

597 Bellouin N., Quaas J., Gryspeerdt E., Kinne S., Stier P., Watson-Parris D., Boucher O.,
598 Carslaw K. S., Christensen M., Daniau A.-L., Dufresne J.-L., Feingold G., Fiedler S., Forster P.,
599 Gettelman A., Haywood J. M., Lohmann U., Malavelle F., Mauritsen T., McCoy D. T., Myhre G.,
600 Mülmenstädt J., Neubauer D., Possner A., Rugenstein M., Sato Y., Schulz M., Schwartz S. E.,
601 Sourdeval O., Storelvmo T., Toll V., Winker D. & Stevens B. Bounding Global Aerosol Radiative
602 Forcing of Climate Change, *Reviews of Geophysics*. 58(1), e2019RG000660,
603 <https://doi.org/10.1029/2019RG000660>, 2020.

604 Bian H., Chin M., Hauglustaine D. A., Schulz M., Myhre G., Bauer S. E., Lund M. T., Karydis
605 V. A., Kucsera T. L., Pan X., Pozzer A., Skeie R. B., Steenrod S. D., Sudo K., Tsigaridis K., Tsimpidi

606 A. P. & Tsyro S. G. Investigation of global particulate nitrate from the AeroCom phase III experiment,
607 *Atmos. Chem. Phys.* 17(21), 12911-12940, 10.5194/acp-17-12911-2017, 2017.

608 Bollasina M. A., Ming Y. & Ramaswamy V. Anthropogenic Aerosols and the Weakening of
609 the South Asian Summer Monsoon, *Science*. 334(6055), 502-505, doi:10.1126/science.1204994, 2011.

610 Chen S., Zhang X., Lin J., Huang J., Zhao D., Yuan T., Huang K., Luo Y., Jia Z., Zang Z., Qiu
611 Y. a. & Xie L. Fugitive Road Dust PM_{2.5} Emissions and Their Potential Health Impacts,
612 *Environmental Science & Technology*. 53(14), 8455-8465, 10.1021/acs.est.9b00666, 2019.

613 Cheng J., Tong D., Liu Y., Yu S., Yan L., Zheng B., Geng G., He K. & Zhang Q. Comparison
614 of Current and Future PM_{2.5} Air Quality in China Under CMIP6 and DPEC Emission Scenarios,
615 *Geophysical Research Letters*. 48(11), e2021GL093197, <https://doi.org/10.1029/2021GL093197>,
616 2021.

617 Cherian R. & Quaas J. Trends in AOD, Clouds, and Cloud Radiative Effects in Satellite Data
618 and CMIP5 and CMIP6 Model Simulations Over Aerosol Source Regions, *Geophysical Research*
619 *Letters*. 47(9), e2020GL087132, <https://doi.org/10.1029/2020GL087132>, 2020.

620 Chowdhury S., Pozzer A., Haines A., Klingmüller K., Münzel T., Paasonen P., Sharma A.,
621 Venkataraman C. & Lelieveld J. Global health burden of ambient PM_{2.5} and the contribution of
622 anthropogenic black carbon and organic aerosols, *Environment International*. 159, 107020,
623 <https://doi.org/10.1016/j.envint.2021.107020>, 2022.

624 Crippa M., Guizzardi D., Muntean M., Schaaf E., Dentener F., van Aardenne J. A., Monni S.,
625 Doering U., Olivier J. G. J., Pagliari V. & Janssens-Maenhout G. Gridded emissions of air pollutants
626 for the period 1970–2012 within EDGAR v4.3.2, *Earth Syst. Sci. Data*. 10(4), 1987-2013,
627 10.5194/essd-10-1987-2018, 2018.

628 Crippa M., Solazzo E., Huang G., Guizzardi D., Koffi E., Muntean M., Schieberle C.,
629 Friedrich R. & Janssens-Maenhout G. High resolution temporal profiles in the Emissions Database for
630 Global Atmospheric Research, *Scientific Data*. 7(1), 121, 10.1038/s41597-020-0462-2, 2020.

631 Crippa M., Guizzardi D., Butler T., Keating T., Kaminski J., Kuenen, J., Kurokawa J., Satoru
632 C., Pouliot G., Racine J., Moran M., Klimont Z., Wu R., Manseau P., Barron H., Smith S., Muntean
633 M., Solazzo E., Banja M., Schaaf E., Pagani F., Monforti F. & Pisoni E. HTAPv3 emission mosaic: a
634 global effort to tackle air quality issues, in preparation., 2022.

635 Elguindi N., Granier C., Stavrou T., Darras S., Bauwens M., Cao H., Chen C., Denier van
636 der Gon H. A. C., Dubovik O., Fu T. M., Henze D. K., Jiang Z., Keita S., Kuenen J. J. P., Kurokawa
637 J., Liousse C., Miyazaki K., Müller J.-F., Qu Z., Solmon F. & Zheng B. Intercomparison of
638 Magnitudes and Trends in Anthropogenic Surface Emissions From Bottom-Up Inventories, Top-
639 Down Estimates, and Emission Scenarios, *Earth's Future*. 8(8), e2020EF001520,
640 <https://doi.org/10.1029/2020EF001520>, 2020.

641 Forster P., Storelvmo T., Armour K., Collins W., Dufresne J.-L., Frame D., Lunt D. J.,
642 Mauritsen T., Palmer M. D., Watanabe M., Wild M. & Zhang H. The Earth's Energy Budget, Climate
643 Feedbacks, and Climate Sensitivity. In *Climate Change 2021: The Physical Science Basis*.
644 Contribution of Working Group I to the Sixth Assessment Report of the Intergovernmental Panel on
645 Climate Change [Masson-Delmotte, V., P. Zhai, A. Pirani, S.L. Connors, C. Péan, S. Berger, N. Caud,
646 Y. Chen, L. Goldfarb, M.I. Gomis, M. Huang, K. Leitzell, E. Lonnoy, J.B.R. Matthews, T.K.
647 Maycock, T. Waterfield, O. Yelekçi, R. Yu, and B. Zhou (eds.)]. Cambridge University Press,
648 Cambridge, United Kingdom and New York, NY, USA, pp. 923–1054,
649 doi:10.1017/9781009157896.009.

650 , 2021.

651 Fricko O., Havlik P., Rogelj J., Klimont Z., Gusti M., Johnson N., Kolp P., Strubegger M.,
652 Valin H., Amann M., Ermolieva T., Forsell N., Herrero M., Heyes C., Kindermann G., Krey V.,
653 McCollum D. L., Obersteiner M., Pachauri S., Rao S., Schmid E., Schoepp W. & Riahi K. The marker
654 quantification of the Shared Socioeconomic Pathway 2: A middle-of-the-road scenario for the 21st
655 century, *Global Environmental Change*. 42, 251-267,
656 <https://doi.org/10.1016/j.gloenvcha.2016.06.004>, 2017.

657 Gliß J., Mortier A., Schulz M., Andrews E., Balkanski Y., Bauer S. E., Benedictow A. M. K.,
658 Bian H., Checa-Garcia R., Chin M., Ginoux P., Griesfeller J. J., Heckel A., Kipling Z., Kirkevåg A.,
659 Kokkola H., Laj P., Le Sager P., Lund M. T., Lund Myhre C., Matsui H., Myhre G., Neubauer D., van

660 Noije T., North P., Olivie D. J. L., Rémy S., Sogacheva L., Takemura T., Tsigaridis K. & Tsyro S. G.
661 AeroCom phase III multi-model evaluation of the aerosol life cycle and optical properties using
662 ground- and space-based remote sensing as well as surface in situ observations, *Atmos. Chem. Phys.*
663 21(1), 87-128, 10.5194/acp-21-87-2021, 2021.

664 Gómez-Sanabria A., Kieseewetter G., Klimont Z., Schoepp W. & Haberl H. Potential for future
665 reductions of global GHG and air pollutants from circular waste management systems, *Nature*
666 *Communications*. 13(1), 106, 10.1038/s41467-021-27624-7, 2022.

667 Gui K., Che H., Wang Y., Xia X., Holben B. N., Goloub P., Cuevas-Agulló E., Yao W.,
668 Zheng Y., Zhao H., Li L. & Zhang X. A global-scale analysis of the MISR Level-3 aerosol optical
669 depth (AOD) product: Comparison with multi-platform AOD data sources, *Atmospheric Pollution*
670 *Research*. 12(12), 101238, <https://doi.org/10.1016/j.apr.2021.101238>, 2021.

671 Hegerl G. C., Brönnimann S., Cowan T., Friedman A. R., Hawkins E., Iles C., Müller W.,
672 Schurer A. & Undorf S. Causes of climate change over the historical record, *Environmental Research*
673 *Letters*. 14(12), 123006, 10.1088/1748-9326/ab4557, 2019.

674 Hoesly R. M., Smith S. J., Feng L., Klimont Z., Janssens-Maenhout G., Pitkanen T., Seibert J.
675 J., Vu L., Andres R. J., Bolt R. M., Bond T. C., Dawidowski L., Kholod N., Kurokawa J. I., Li M., Liu
676 L., Lu Z., Moura M. C. P., O'Rourke P. R. & Zhang Q. Historical (1750–2014) anthropogenic
677 emissions of reactive gases and aerosols from the Community Emission Data System (CEDS), *Geosci.*
678 *Model Dev*. 2018(11), 369-408, <https://doi.org/10.5194/gmd-11-369-2018>, 2018.

679 Holben B. N., Eck T. F., Slutsker I., Tanré D., Buis J. P., Setzer A., Vermote E., Reagan J. A.,
680 Kaufman Y. J., Nakajima T., Lavenu F., Jankowiak I. & Smirnov A. AERONET—A Federated
681 Instrument Network and Data Archive for Aerosol Characterization, *Remote Sensing of Environment*.
682 66(1), 1-16, [https://doi.org/10.1016/S0034-4257\(98\)00031-5](https://doi.org/10.1016/S0034-4257(98)00031-5), 1998.

683

684 Kanaya Y., Yamaji K., Miyakawa T., Taketani F., Zhu C., Choi Y., Komazaki Y., Ikeda K.,
685 Kondo Y. & Klimont Z. Rapid reduction in black carbon emissions from China: evidence from 2009–
686 2019 observations on Fukue Island, Japan, *Atmos. Chem. Phys.* 20(11), 6339-6356, 10.5194/acp-20-
687 6339-2020, 2020.

688 Klimont Z., Smith S. J. & Cofala J. The last decade of global anthropogenic sulfur dioxide:
689 2000–2011 emissions, *Environmental Research Letters*. 8(1), 014003, 10.1088/1748-
690 9326/8/1/014003, 2013.

691 Klimont Z., Kupiainen K., Heyes C., Purohit P., Cofala J., Rafaj P., Borken-Kleefeld J. &
692 Schöpp W. Global anthropogenic emissions of particulate matter including black carbon, *Atmos.*
693 *Chem. Phys.* 17(14), 8681-8723, 10.5194/acp-17-8681-2017, 2017.

694 Korhonen H., Carslaw K. S., Forster P. M., Mikkonen S., Gordon N. D. & Kokkola H.
695 Aerosol climate feedback due to decadal increases in Southern Hemisphere wind speeds, *Geophysical*
696 *Research Letters*. 37(2), <https://doi.org/10.1029/2009GL041320>, 2010.

697 Kurokawa J. & Ohara T. Long-term historical trends in air pollutant emissions in Asia:
698 Regional Emission inventory in ASia (REAS) version 3, *Atmos. Chem. Phys.* 20(21), 12761-12793,
699 10.5194/acp-20-12761-2020, 2020.

700 Levy R. C., Remer L. A., Kleidman R. G., Mattoo S., Ichoku C., Kahn R. & Eck T. F. Global
701 evaluation of the Collection 5 MODIS dark-target aerosol products over land, *Atmos. Chem. Phys.*
702 10(21), 10399-10420, 10.5194/acp-10-10399-2010, 2010.

703 Li C., McLinden C., Fioletov V., Krotkov N., Carn S., Joiner J., Streets D., He H., Ren X., Li
704 Z. & Dickerson R. R. India Is Overtaking China as the World's Largest Emitter of Anthropogenic
705 Sulfur Dioxide, *Scientific Reports*. 7(1), 14304, 10.1038/s41598-017-14639-8, 2017.

706 Lund M. T., Myhre G., Haslerud A. S., Skeie R. B., Griesfeller J., Platt S. M., Kumar R.,
707 Myhre C. L. & Schulz M. Concentrations and radiative forcing of anthropogenic aerosols from 1750
708 to 2014 simulated with the Oslo CTM3 and CEDS emission inventory, *Geosci. Model Dev*. 11(12),
709 4909-4931, 10.5194/gmd-11-4909-2018, 2018.

710 Lund M. T., Myhre G. & Samset B. H. Anthropogenic aerosol forcing under the Shared
711 Socioeconomic Pathways, *Atmos. Chem. Phys.* 19(22), 13827-13839, 10.5194/acp-19-13827-2019,
712 2019.

713 Lund M. T., Aamaas B., Stjern C. W., Klimont Z., Berntsen T. K. & Samset B. H. A
714 continued role of short-lived climate forcers under the Shared Socioeconomic Pathways, *Earth Syst.*
715 *Dynam.* 11(4), 977-993, 10.5194/esd-11-977-2020, 2020.

716 Marvel K., Biasutti M. & Bonfils C. Fingerprints of external forcings on Sahel rainfall:
717 aerosols, greenhouse gases, and model-observation discrepancies, *Environmental Research Letters.*
718 15(8), 084023, 10.1088/1748-9326/ab858e, 2020.

719 MOD08 MODIS Level 3 Atmosphere Products (MOD 08), Data Products Handbook Volume
720 2. https://modis.gsfc.nasa.gov/data/dataproduct/dataproducts.php?MOD_NUMBER=08 (accessed
721 04/26/2018), 2018.

722 Mortier A., Gliß J., Schulz M., Aas W., Andrews E., Bian H., Chin M., Ginoux P., Hand J.,
723 Holben B., Zhang H., Kipling Z., Kirkevåg A., Laj P., Lurton T., Myhre G., Neubauer D., Olivie D.,
724 von Salzen K., Skeie R. B., Takemura T. & Tilmes S. Evaluation of climate model aerosol trends with
725 ground-based observations over the last 2 decades – an AeroCom and CMIP6 analysis, *Atmos. Chem.*
726 *Phys.* 20(21), 13355-13378, 10.5194/acp-20-13355-2020, 2020.

727 Moseid K. O., Schulz M., Storelvmo T., Julsrud I. R., Olivie D., Nabat P., Wild M., Cole J. N.
728 S., Takemura T., Oshima N., Bauer S. E. & Gastineau G. Bias in CMIP6 models as compared to
729 observed regional dimming and brightening, *Atmos. Chem. Phys.* 20(24), 16023-16040, 10.5194/acp-
730 20-16023-2020, 2020.

731 Myhre G., Samset B. H., Schulz M., Balkanski Y., Bauer S., Berntsen T. K., Bian H., Bellouin
732 N., Chin M., Diehl T., Easter R. C., Feichter J., Ghan S. J., Hauglustaine D., Iversen T., Kinne S.,
733 Kirkevåg A., Lamarque J. F., Lin G., Liu X., Lund M. T., Luo G., Ma X., van Noije T., Penner J. E.,
734 Rasch P. J., Ruiz A., Seland Ø., Skeie R. B., Stier P., Takemura T., Tsigaridis K., Wang P., Wang Z.,
735 Xu L., Yu H., Yu F., Yoon J. H., Zhang K., Zhang H. & Zhou C. Radiative forcing of the direct
736 aerosol effect from AeroCom Phase II simulations, *Atmos. Chem. Phys.* 13(4), 1853-1877,
737 10.5194/acp-13-1853-2013, 2013.

738 Myhre G., Aas W., Cherian R., Collins W., Faluvegi G., Flanner M., Forster P., Hodnebrog
739 Ø., Klimont Z., Lund M. T., Mülmenstädt J., Lund Myhre C., Olivie D., Prather M., Quaas J., Samset
740 B. H., Schnell J. L., Schulz M., Shindell D., Skeie R. B., Takemura T. & Tsyro S. Multi-model
741 simulations of aerosol and ozone radiative forcing due to anthropogenic emission changes during the
742 period 1990–2015, *Atmos. Chem. Phys.* 17(4), 2709-2720, 10.5194/acp-17-2709-2017, 2017.

743 O'Rourke P. R., Smith S. J., Mott A., Ahsan H., McDuffie E. E., Crippa M., Klimont S.,
744 McDonald B., Wang Z., Nicholson M. B., Feng L. & Hoesly R. M. (2021), CEDS v-2021-02-05
745 Emission Data 1975-2019 (Version Feb-05-2021), edited, Zenodo.

746 Paulot F., Paynter D., Ginoux P., Naik V. & Horowitz L. W. Changes in the aerosol direct
747 radiative forcing from 2001 to 2015: observational constraints and regional mechanisms, *Atmos.*
748 *Chem. Phys.* 18(17), 13265-13281, 10.5194/acp-18-13265-2018, 2018.

749 Paulot F., Paynter D., Winton M., Ginoux P., Zhao M. & Horowitz L. W. Revisiting the
750 Impact of Sea Salt on Climate Sensitivity, *Geophysical Research Letters.* 47(3), e2019GL085601,
751 <https://doi.org/10.1029/2019GL085601>, 2020.

752 Persad G. G., Samset B. H. & Wilcox L. J. Comment: Aerosols must be included in climate
753 risk assessments, *Nature.* 611, 662-664, 2022.

754 Quaas J., Boucher O. & Lohmann U. Constraining the total aerosol indirect effect in the
755 LMDZ and ECHAM4 GCMs using MODIS satellite data, *Atmos. Chem. Phys.* 6(4), 947-955,
756 10.5194/acp-6-947-2006, 2006.

757 Quaas J., Jia H., Smith C., Albright A. L., Aas W., Bellouin N., Boucher O., Doutriaux-
758 Boucher M., Forster P. M., Grosvenor D., Jenkins S., Klimont Z., Loeb N. G., Ma X., Naik V., Paulot
759 F., Stier P., Wild M., Myhre G. & Schulz M. Robust evidence for reversal in the aerosol effective
760 climate forcing trend, *Atmos. Chem. Phys. Discuss.* 2022, 1-25, 10.5194/acp-2022-295, 2022.

761 Ramachandran S., Rupakheti M. & Cherian R. Insights into recent aerosol trends over Asia
762 from observations and CMIP6 simulations, *Science of The Total Environment.* 807, 150756,
763 <https://doi.org/10.1016/j.scitotenv.2021.150756>, 2022.

764 Randerson J. T., van der Werf G. R., Giglio L., Collatz G. J. & Kasibhatla P. S. Global Fire
765 Emissions Database, Version 4.1 (GFEDv4). ORNL DAAC, Oak Ridge, Tennessee, USA. ,
766 <https://doi.org/10.3334/ORNLDAAC/1293>, 2017.

767 Regayre L. A., Pringle K. J., Booth B. B. B., Lee L. A., Mann G. W., Browse J., Woodhouse
768 M. T., Rap A., Reddington C. L. & Carslaw K. S. Uncertainty in the magnitude of aerosol-cloud
769 radiative forcing over recent decades, *Geophysical Research Letters*. 41(24), 9040-9049,
770 <https://doi.org/10.1002/2014GL062029>, 2014.

771 Samset B. H., Sand M., Smith C. J., Bauer S. E., Forster P. M., Fuglestedt J. S., Osprey S. &
772 Schleussner C.-F. Climate Impacts From a Removal of Anthropogenic Aerosol Emissions,
773 *Geophysical Research Letters*. 45(2), 1020-1029, <https://doi.org/10.1002/2017GL076079>, 2018.

774 Samset B. H., Lund M. T., Bollasina M., Myhre G. & Wilcox L. Emerging Asian aerosol
775 patterns, *Nature Geoscience*. 12(8), 582-584, 10.1038/s41561-019-0424-5, 2019.

776 SCPRC The State Council Issues Action Plan on Prevention and Control of Air Pollution
777 Introducing Ten Measures to Improve Air Quality.
778 https://english.mee.gov.cn/News_service/infocus/201309/t20130924_260707.shtml (Accessed
779 22/01/20), 2013.

780 SCPRC The State Council rolls out a three-year action plan for clean air.
781 https://english.mee.gov.cn/News_service/news_release/201807/t20180713_446624.shtml (Accessed
782 22/01/20), 2018.

783 Sherman J. P., Gupta P., Levy R. C. & Sherman P. J. An Evaluation of MODIS-Retrieved
784 Aerosol Optical Depth over a Mountainous AERONET Site in the Southeastern US, *Aerosol and Air
785 Quality Research*. 16(12), 3243-3255, 10.4209/aaqr.2015.09.0568, 2017.

786 Sillmann J., Pozzoli L., Vignati E., Kloster S. & Feichter J. Aerosol effect on climate extremes
787 in Europe under different future scenarios, *Geophysical Research Letters*. 40(10), 2290-2295,
788 <https://doi.org/10.1002/grl.50459>, 2013.

789 Smith S. J., McDuffie E. E. & Charles M. Opinion: Coordinated development of emission
790 inventories for climate forcers and air pollutants, *Atmos. Chem. Phys.* 22(19), 13201-13218,
791 10.5194/acp-22-13201-2022, 2022.

792 Stamnes K., Tsay S. C., Wiscombe W. & Jayaweera K. Numerically stable algorithm for
793 discrete-ordinate-method radiative transfer in multiple scattering and emitting layered media, *Appl.
794 Opt.* 27(12), 2502-2509, 10.1364/AO.27.002502, 1988.

795 Struthers H., Ekman A. M. L., Glantz P., Iversen T., Kirkevåg A., Seland Ø., Mårtensson E.
796 M., Noone K. & Nilsson E. D. Climate-induced changes in sea salt aerosol number emissions: 1870 to
797 2100, *Journal of Geophysical Research: Atmospheres*. 118(2), 670-682,
798 <https://doi.org/10.1002/jgrd.50129>, 2013.

799 Su W., Liang L., Myhre G., Thorsen T. J., Loeb N. G., Schuster G. L., Ginoux P., Paulot F.,
800 Neubauer D., Checa-Garcia R., Matsui H., Tsigaridis K., Skeie R. B., Takemura T., Bauer S. E. &
801 Schulz M. Understanding Top-of-Atmosphere Flux Bias in the AeroCom Phase III Models: A Clear-
802 Sky Perspective, *Journal of Advances in Modeling Earth Systems*. 13(9), e2021MS002584,
803 <https://doi.org/10.1029/2021MS002584>, 2021.

804 Szopa S., Naik V., Adhikary B., Artaxo P., Berntsen T., Collins W. D., Fuzzi S., Gallardo L.,
805 Kiendler Scharr A., Klimont Z., Liao H., Unger N. & Zanis P. Short-Lived Climate Forcers. In:
806 Climate Change 2021: The Physical Science Basis. Contribution of Working Group I to the Sixth
807 Assessment Report of the Intergovernmental Panel on Climate Change [Masson-Delmotte, V., P. Zhai,
808 A. Pirani, S. L. Connors, C. Péan, S. Berger, N. Caud, Y. Chen, L. Goldfarb, M. I. Gomis, M. Huang,
809 K. Leitzell, E. Lonnoy, J. B. R. Matthews, T. K. Maycock, T. Waterfield, O. Yelekçi, R. Yu and B.
810 Zhou (eds.)]. Cambridge University Press, Cambridge, United Kingdom and New York, NY, USA,
811 pp. 817–922 doi:10.1017/9781009157896.008, 2021.

812 Søvde O. A., Prather M. J., Isaksen I. S. A., Berntsen T. K., Stordal F., Zhu X., Holmes C. D.
813 & Hsu J. The chemical transport model Oslo CTM3, *Geosci. Model Dev.* 5(6), 1441-1469,
814 10.5194/gmd-5-1441-2012, 2012.

815 Tong D., Cheng J., Liu Y., Yu S., Yan L., Hong C., Qin Y., Zhao H., Zheng Y., Geng G., Li
816 M., Liu F., Zhang Y., Zheng B., Clarke L. & Zhang Q. Dynamic projection of anthropogenic
817 emissions in China: methodology and 2015–2050 emission pathways under a range of socio-
818 economic, climate policy, and pollution control scenarios, *Atmos. Chem. Phys.* 20(9), 5729-5757,
819 10.5194/acp-20-5729-2020, 2020.

820 van Marle M. J. E., Kloster S., Magi B. I., Marlon J. R., Daniau A. L., Field R. D., Arneth A.,
821 Forrest M., Hantson S., Kehrwald N. M., Knorr W., Lasslop G., Li F., Mangeon S., Yue C., Kaiser J.

822 W. & van der Werf G. R. Historic global biomass burning emissions for CMIP6 (BB4CMIP) based on
823 merging satellite observations with proxies and fire models (1750–2015), *Geosci. Model Dev.* 10(9),
824 3329-3357, 10.5194/gmd-10-3329-2017, 2017.

825 Vogel A., Alessa G., Scheele R., Weber L., Dubovik O., North P. & Fiedler S. Uncertainty in
826 Aerosol Optical Depth From Modern Aerosol-Climate Models, Reanalyses, and Satellite Products,
827 *Journal of Geophysical Research: Atmospheres.* 127(2), e2021JD035483,
828 <https://doi.org/10.1029/2021JD035483>, 2022.

829 Wang C.-S., Wang Z.-L., Lei Y.-D., Zhang H., Che H.-Z. & Zhang X.-Y. Differences in East
830 Asian summer monsoon responses to Asian aerosol forcing under different emission inventories,
831 *Advances in Climate Change Research*, <https://doi.org/10.1016/j.accr.2022.02.008>, 2022.

832 Wang Z., Lin L., Xu Y., Che H., Zhang X., Zhang H., Dong W., Wang C., Gui K. & Xie B.
833 Incorrect Asian aerosols affecting the attribution and projection of regional climate change in CMIP6
834 models, *npj Climate and Atmospheric Science.* 4(1), 2, 10.1038/s41612-020-00159-2, 2021.

835 Wiedinmyer C., Yokelson R. J. & Gullett B. K. Global Emissions of Trace Gases, Particulate
836 Matter, and Hazardous Air Pollutants from Open Burning of Domestic Waste, *Environmental Science*
837 *& Technology.* 48(16), 9523-9530, 10.1021/es502250z, 2014.

838 Womack C. C., McDuffie E. E., Edwards P. M., Bares R., de Gouw J. A., Docherty K. S.,
839 Dubé W. P., Fibiger D. L., Franchin A., Gilman J. B., Goldberger L., Lee B. H., Lin J. C., Long R.,
840 Middlebrook A. M., Millet D. B., Moravek A., Murphy J. G., Quinn P. K., Riedel T. P., Roberts J. M.,
841 Thornton J. A., Valin L. C., Veres P. R., Whitehill A. R., Wild R. J., Warneke C., Yuan B., Baasandorj
842 M. & Brown S. S. An Odd Oxygen Framework for Wintertime Ammonium Nitrate Aerosol Pollution
843 in Urban Areas: NO_x and VOC Control as Mitigation Strategies, *Geophysical Research Letters.* 46(9),
844 4971-4979, <https://doi.org/10.1029/2019GL082028>, 2019.

845 Wu C., Venevsky S., Sitch S., Mercado L. M., Huntingford C. & Staver A. C. Historical and
846 future global burned area with changing climate and human demography, *One Earth.* 4(4), 517-530,
847 <https://doi.org/10.1016/j.oneear.2021.03.002>, 2021.

848 Xia W., Wang Y., Chen S., Huang J., Wang B., Zhang G. J., Zhang Y., Liu X., Ma J., Gong
849 P., Jiang Y., Wu M., Xue J., Wei L. & Zhang T. Double Trouble of Air Pollution by Anthropogenic
850 Dust, *Environmental Science & Technology.* 56(2), 761-769, 10.1021/acs.est.1c04779, 2022.

851 Yang S., Yuan B., Peng Y., Huang S., Chen W., Hu W., Pei C., Zhou J., Parrish D. D., Wang
852 W., He X., Cheng C., Li X. B., Yang X., Song Y., Wang H., Qi J., Wang B., Wang C., Wang C.,
853 Wang Z., Li T., Zheng E., Wang S., Wu C., Cai M., Ye C., Song W., Cheng P., Chen D., Wang X.,
854 Zhang Z., Wang X., Zheng J. & Shao M. The formation and mitigation of nitrate pollution:
855 comparison between urban and suburban environments, *Atmos. Chem. Phys.* 22(7), 4539-4556,
856 10.5194/acp-22-4539-2022, 2022.

857 Zhai S., Jacob D. J., Wang X., Liu Z., Wen T., Shah V., Li K., Moch J. M., Bates K. H., Song
858 S., Shen L., Zhang Y., Luo G., Yu F., Sun Y., Wang L., Qi M., Tao J., Gui K., Xu H., Zhang Q., Zhao
859 T., Wang Y., Lee H. C., Choi H. & Liao H. Control of particulate nitrate air pollution in China, *Nature*
860 *Geoscience.* 14(6), 389-395, 10.1038/s41561-021-00726-z, 2021.

861 Zheng B., Tong D., Li M., Liu F., Hong C., Geng G., Li H., Li X., Peng L., Qi J., Yan L.,
862 Zhang Y., Zhao H., Zheng Y., He K. & Zhang Q. Trends in China's anthropogenic emissions since
863 2010 as the consequence of clean air actions, *Atmos. Chem. Phys.* 18(19), 14095-14111, 10.5194/acp-
864 18-14095-2018, 2018.

865 Aas W., Mortier A., Bowersox V., Cherian R., Faluvegi G., Fagerli H., Hand J., Klimont Z.,
866 Galy-Lacaux C., Lehmann C. M. B., Myhre C. L., Myhre G., Olivié D., Sato K., Quaas J., Rao P. S.
867 P., Schulz M., Shindell D., Skeie R. B., Stein A., Takemura T., Tsyro S., Vet R. & Xu X. Global and
868 regional trends of atmospheric sulfur, *Scientific Reports.* 9(1), 953, 10.1038/s41598-018-37304-0,
869 2019.

870

871

872

873

874
875
876
877
878
879
880
881
882
883
884
885
886
887
888
889
890
891
892
893
894
895
896
897
898
899
900

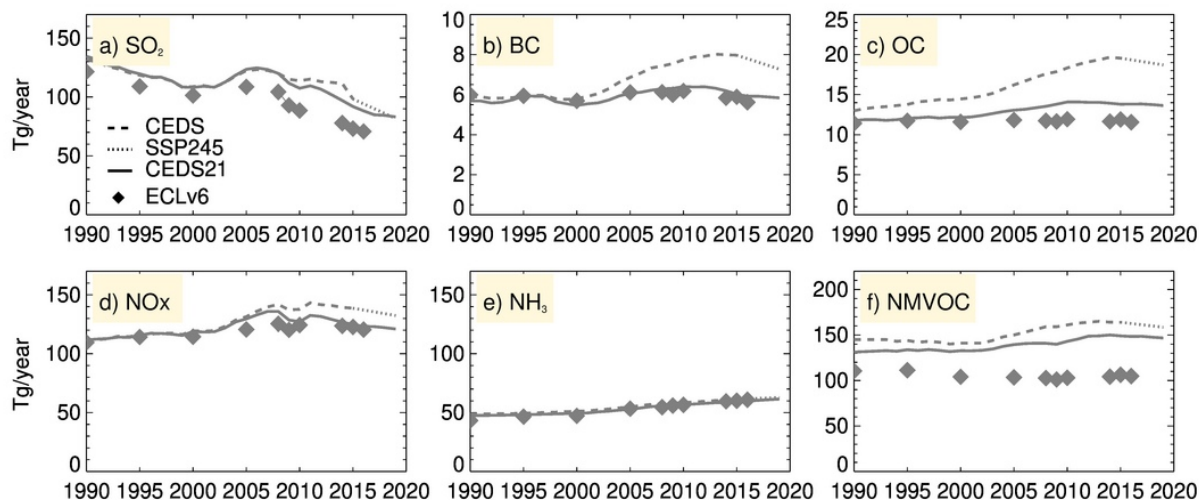
Tables:

Table 1: Summary of experiments used in the study.

Name	Description	Years simulated
CEDS	CEDS v2016 emissions, fixed meteorology	1990, 1995, 2000, 2005, 2010 2014
CEDS21	CEDS v2021 emissions, fixed meteorology	1990, 1995, 2000, 2005, 2010 2014, 2016, 2018, 2019
ECLv6	ECLIPSEv6b emissions, fixed meteorology	1990, 1995, 2000, 2005, 2010 2014, 2016
CEDSmet	CEDS v2017 emissions until 2014 and SSP2-4.5 for 2015-2017, running meteorology	1990-2017
CEDS21met	CEDS v2021 emissions, running meteorology	2001-2017

901 **Figures:**

902

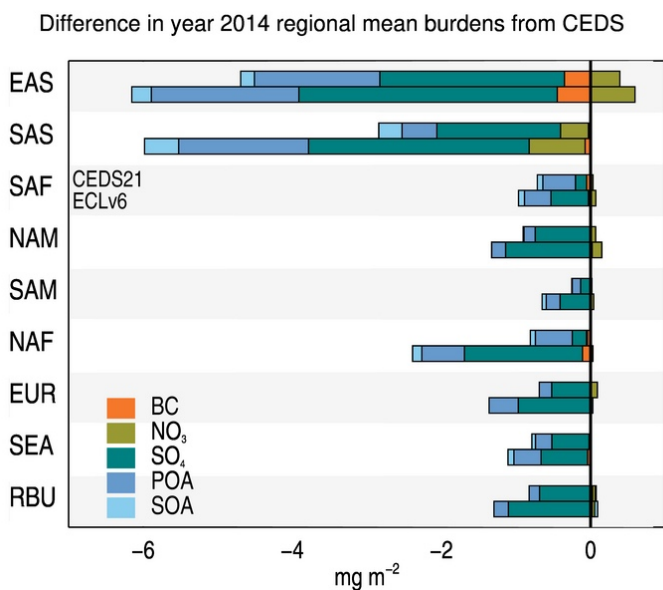


903

904 **Figure 1** Global total anthropogenic emissions of SO_2 , BC , OC , NO_x , NH_3 , and $NMVOC$ in the *CEDS21*,
905 *ECLv6*, *CEDS17* inventories, for the period 1990 to the most recent inventory year (2019, 2016 and
906 2014, respectively). Dotted lines show emissions from the *SSP2-4.5* scenario, linearly interpolated from
907 2015 to 2019.

908

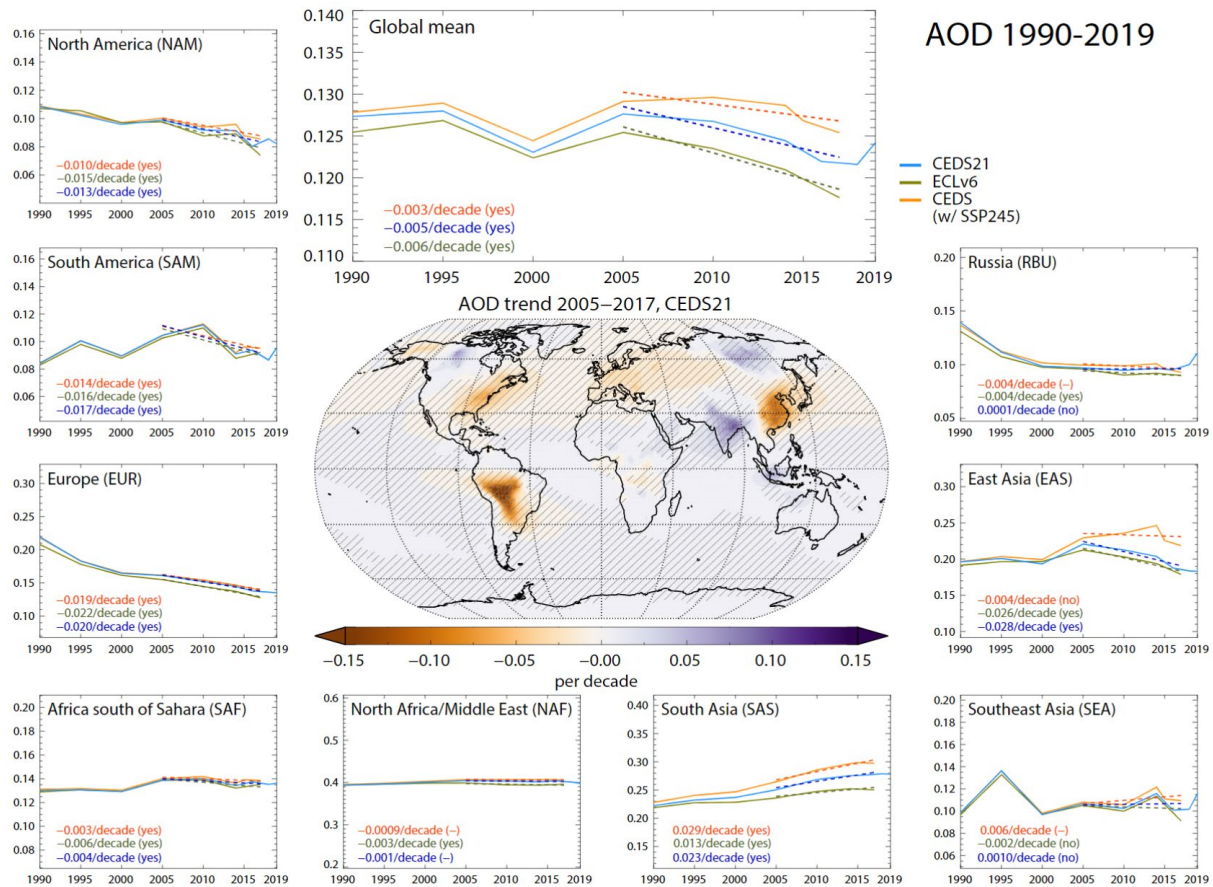
909



910

911 **Figure 2** Absolute difference in regional mean burden of the key anthropogenic aerosol species between
912 simulations with *CEDS21* and *CEDS* (upper bar) and *ECLv6* and *CEDS* (lower bar). Regions are the
913 same as in Lund et al. (2019): *EAS* = East Asia, *SAS* = South Asia, *SAF* = Sub-Saharan Africa, *NAM* =
914 North America, *SAM* = South America, *NAF* = North Africa and the Middle East, *EUR* = Europe, *SEA*
915 = South East Asia, *RBU* = Russia.

916



917

918

919 *Figure 3: Global and regional mean total AOD simulated with emissions from the CEDS21, ECLv6 and*
 920 *CEDS inventories. In the case of CEDS, the timeseries is extended from 2014 to 2017 using SSP2-4.5*
 921 *emissions. Dashed lines show the linear 2005-2017 trend, defined as statistically significant from no*
 922 *trend when the linear Pearson's correlation coefficient is significant at the 0.05 level. To reduce any*
 923 *influence of individual, outlier years on the trends, we calculate a set of trends removing one-and-one*
 924 *year from the sample and show the average. Significance is given in the parenthesis. If a dash is given,*
 925 *individual trends from the sample differed from each other in terms of significance.*

926

927

928

929

930

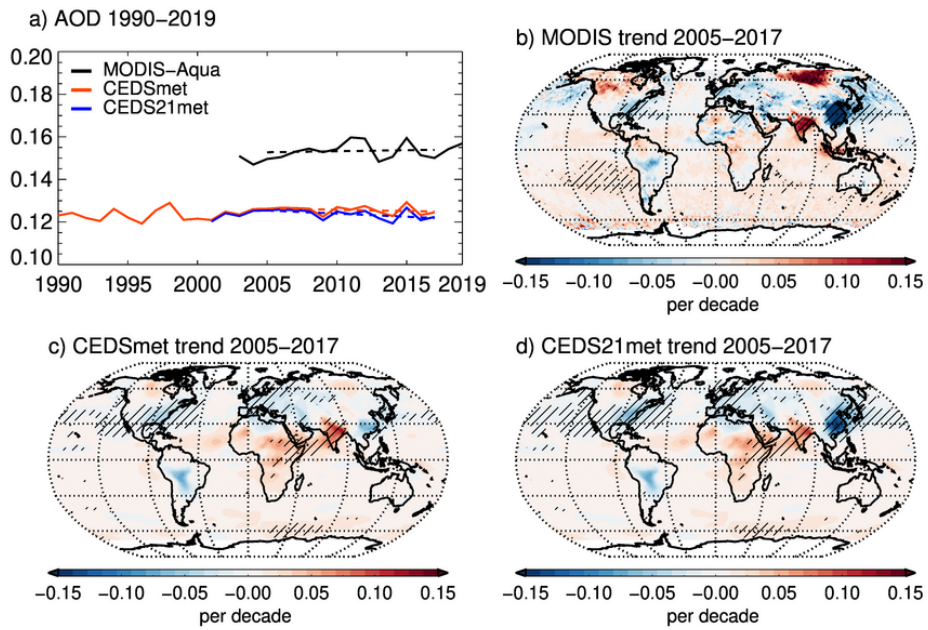
931

932

933

934

935



936

937

938 *Figure 4: a) Global, annual mean AOD from MODIS-Aqua and the OsloCTM3 over the 1990-2019*
 939 *period. Note that data north and south of 70° is excluded here due to the limited MODIS-Aqua coverage.*
 940 *Dashed lines show linear trend from 2005 to 2017. b-d) Spatially resolved linear trends in observed and*
 941 *simulated AOD. Hatching indicates where the linear trend is significantly different from zero at the 0.05*
 942 *level.*

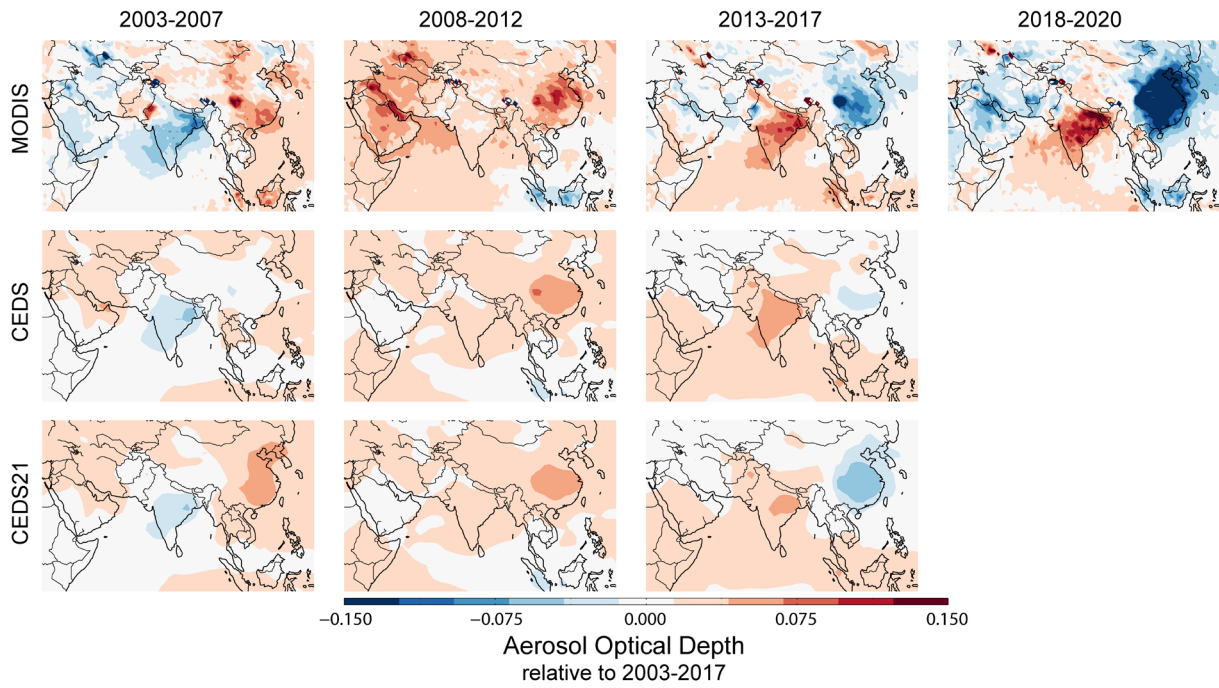
943

944

945

946

947



948

949 *Figure 5: Evolution of AOD over South and East Asia, and the Middle East, over the period 2003-*
 950 *2020. All panels show five-year average deviations from the period 2003-2017, except the rightmost*
 951 *MODIS-Aqua panel which show the three-year average deviation (same baseline). The top row shows*
 952 *retrievals from MODIS Aqua; the two bottom rows show model calculations with OsloCTM3 based on*
 953 *the CEDS and CEDS21 emission inventories.*

954

955

956

957

958

959

960

961

962

963

964

965

966

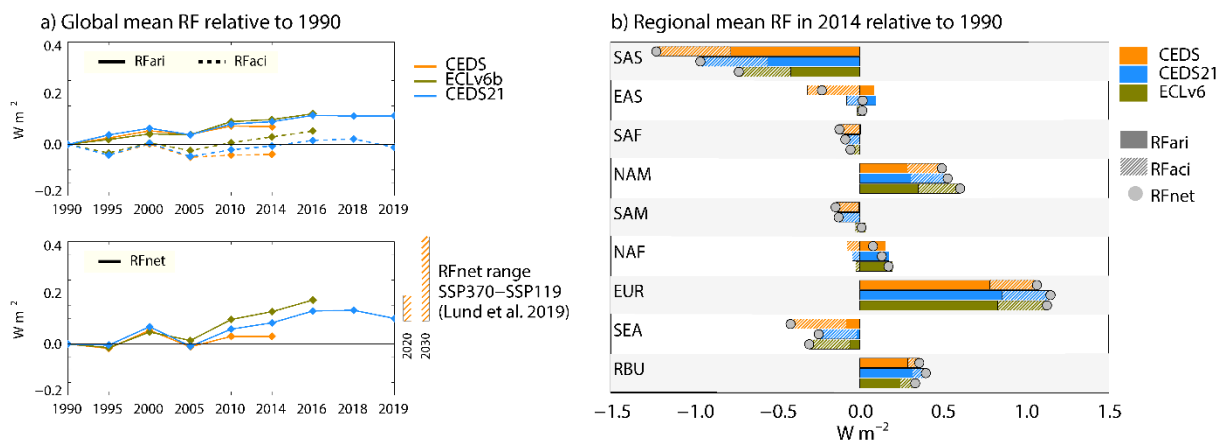
967

968

969

970

971



972

973

974 *Figure 6: a) Global mean RFari and RFaci (top) and RFnet (RFari+RFaci) (bottom) relative to 1990*
975 *from simulations using the CEDS, CEDS21, and ECLv6 emission inventories. The vertical bars to the*
976 *right show the range in RFnet in 2020 and 2030 (relative to 1990) estimated with the SSP1-1.9 and*
977 *SSP3-7.0 emissions (adapted from Lund et al. (2019)). b) Regional mean RFnet, RFari, and RFaci in*
978 *2014 relative to 1990 in simulations with CEDS, CEDS21, and ECLv6 inventories.*

979